



POLITECNICO
MILANO 1863

RE.PUBLIC@POLIMI

Research Publications at Politecnico di Milano

Post-Print

This is the accepted version of:

C. Vergara, D. Le Van, M. Quadrio, L. Formaggia, M. Domanin
Large Eddy Simulations of Blood Dynamics in Abdominal Aortic Aneurysms
Medical Engineering and Physics, Vol. 47, 2017, p. 38-46
doi:10.1016/j.medengphy.2017.06.030

The final publication is available at <https://doi.org/10.1016/j.medengphy.2017.06.030>

Access to the published version may require subscription.

When citing this work, cite the original published paper.

© 2017. This manuscript version is made available under the CC-BY-NC-ND 4.0 license
<http://creativecommons.org/licenses/by-nc-nd/4.0/>

Permanent link to this version

<http://hdl.handle.net/11311/1029553>

Large Eddy Simulations of blood dynamics in abdominal aortic aneurysms

Christian Vergara^{a,*}, Davide Le Van^a, Maurizio Quadrio^b, Luca Formaggia^a, Maurizio Domanin^c

^a*MOX, Dipartimento di Matematica, Politecnico di Milano, Italy*

^b*Dipartimento di Scienze e Tecnologie Aerospaziali, Politecnico di Milano, Italy*

^c*Operative Unit of Vascular Surgery, Fondazione I.R.C.C.S. Ca' Granda Ospedale Maggiore Policlinico di Milano, Italy and
Department of Clinical Sciences and Community, Università di Milano, Italy*

Abstract

We study the effects of transition to turbulence in abdominal aortic aneurysms (AAA). The presence of transitional effects in such districts is related to the heart pulsatility and the sudden change of diameter of the vessels, and has been recorded by means of clinical measures as well as of computational studies. Here we propose, for the first time, the use of a large eddy simulation (LES) model to accurately describe transition to turbulence in realistic scenarios of AAA obtained from radiological images. To this aim, we post-process the obtained numerical solutions to assess significant quantities, such as the ensemble-averaged velocity and wall shear stress, the standard deviation of the fluctuating velocity field, and vortical structures deduced via the so-called Q-criterion. The results demonstrate the suitability of the considered LES model and show the presence of significant transitional effects around the impingement region during the mid-deceleration phase.

Keywords: Abdominal aortic aneurysm, large eddy simulation, ensemble-average, transition to turbulence

1. Introduction

Dynamics of blood plays a major role in the development of abdominal aortic aneurysms (AAA), an enlargement of the abdominal aorta whose rupture could lead to fatal events [1]. In particular, specific wall shear stress (WSS) conditions regulate the production of nitric oxide [2], which is known to cause the loss of elastin which is at the root of aneurysm formation and growth; cause the activation of blood platelets [3], playing a central role in thrombus formation; and are responsible for anisotropic displacements of the aneurysmatic sac [4].

In this context, the possibility for the flow regime to be transitional or turbulent owing to the enlargement of the lumen and to pulsatility [5, 6] has a strong impact on WSS and thus on the above-mentioned relationships. In particular, turbulence effects are responsible for an increased platelets activation [7] and damage of the blood cell [8], and provide additional mechanical stresses that may lead to further AAA dilatation [9]. Although not determined mainly by WSS, also the rupture process may be influenced by turbulence in the aneurysm, since the corresponding arterial wall vibration may damage the structural components of the wall [10].

For these reasons, the inclusion of turbulence effects (via turbulence models, or the use of very fine meshes) is mandatory for a computational study of blood dynamics in AAA and for an accurate description of the aneurysm evolution [10, 9, 11]. One major issue relies on the qualification and quantification of

*Corresponding author

Email addresses: christian.vergara@polimi.it (Christian Vergara), davide.le@mail.polimi.it (Davide Le Van), maurizio.quadrio@polimi.it (Maurizio Quadrio), luca.formaggia@polimi.it (Luca Formaggia), maurizio.domanin@unimi.it (Maurizio Domanin)

turbulence, since its very definition is in general problematic, and particularly so in hemodynamics. Indeed, in this context turbulence does not fully develop since the acceleration at the beginning of a new heartbeat laminarizes the flow which thus can only experience a transitional behavior [8]. This is a common fact in vascular hemodynamics, for example in stenotic carotids [12, 13, 14, 15] and cerebral aneurysms [16, 17]. Often, some authors describe with the term "turbulent" blood flows which are simply unsteady and/or vortical. Only few computational studies have introduced suitable statistically-based quantities to assess turbulence effects in AAA [10, 11].

In this work, we consider *large eddy simulations* (LES) for the study of transition to turbulence effects in AAA. In particular, we apply the eddy-viscosity σ -model [18] to three patient-specific geometries. To assess turbulence effects, we study the standard deviation of the velocity field, the ratio between eddy and molecular viscosities, and the fluctuations of the kinetic energy. Our results show the suitability of LES models in hemodynamics and the presence of a significant amount of transitional effects localized close to the jet impingement region during the deceleration phase.

2. Materials and Methods

2.1. Geometric data

THREE PATIENTS (DENOTED P1, P2, AND P3 IN WHAT FOLLOWS) WHO UNDERWENT 4D-CT AS PREOPERATIVE EVALUATION OF AN AAA WERE SELECTED FOR INCLUSION IN THE PRESENT STUDY, WHICH WAS APPROVED BY THE ETHICAL REVIEW BOARD OF THE HOSPITAL WHERE THE PATIENTS WERE TREATED. THE PATIENTS GAVE INFORMED CONSENT. The radiological acquisitions were performed with a Somatom Definition Dual Source CT (Siemens, Erlangen, Germany), before and after contrast media administration with retrospectively electrocardiographic (ECG) gated spiral acquisition. Non-ionic contrast media (Iomeron, Bracco, Milan, Italy) was used with a concentration of 400 mg/I mg, 1.5 cc pro kg, and an injection speed of 3 cc/s. The temporal resolution was 85 ms, and the total effective dose according to the applied protocol was 34 mSv per acquisition and per patient.

The 3D geometric reconstructions were performed by means of the Vascular Modeling Toolkit, VMTK [19]. The 3D surface model of the lumen surface of the abdominal aorta was reconstructed using a gradient-driven level set technique. Then, the surface models of the three geometries were turned into volumetric meshes of linear tetrahedra, with three thin layers close to the wall. In particular, the meshes were formed by 275k and 110k tetrahedra for P1, 115k tetraedra for P2, and 120k tetraedra for P3. These values correspond to a characteristic space discretization parameter $h = 0.08\text{ cm}$ and $h = 0.11\text{ cm}$ for P1, and $h = 0.13\text{ cm}$ for P2 and P3.

2.2. Numerical methods

Blood is modelled as a constant density, Newtonian and homogeneous fluid, a well accepted hypothesis for medium and large vessels [20].

LES models are based on the decomposition of the fluid unknowns in resolved and unresolved quantities, $[\bar{\mathbf{u}}, \bar{p}]$ and $[\mathbf{u}', p']$, respectively, so that $\mathbf{u} = \bar{\mathbf{u}} + \mathbf{u}'$ and $p = \bar{p} + p'$ [21]. The resolved quantities are referred to as *filtered*. To derive a set of equations for $\bar{\mathbf{u}}$ and \bar{p} , a formal filtering procedure is applied to the Navier–Stokes equations. Defining the *subgrid-scale* tensor $\boldsymbol{\tau} = \overline{\mathbf{u} \otimes \mathbf{u}} - \bar{\mathbf{u}} \otimes \bar{\mathbf{u}}$, which models the effect of the unresolved scales on the resolved ones [22, 23], we consider the following filtered Navier–Stokes problem (normalized over the fluid density):

Find the velocity $\bar{\mathbf{u}}(t, \mathbf{x})$ and the pressure $\bar{p}(t, \mathbf{x})$ such that

$$\frac{\partial \bar{\mathbf{u}}}{\partial t} - \nu \nabla \cdot \mathbf{S}(\bar{\mathbf{u}}) + \nabla \cdot (\bar{\mathbf{u}} \otimes \bar{\mathbf{u}}) + \nabla \bar{p} + \nabla \cdot \boldsymbol{\tau}^d(\bar{\mathbf{u}}) = \mathbf{0} \quad t \in (0, MT], \mathbf{x} \in \Omega, \quad (1a)$$

$$\nabla \cdot \bar{\mathbf{u}} = 0 \quad t \in (0, MT], \mathbf{x} \in \Omega, \quad (1b)$$

$$\bar{\mathbf{u}} = \mathbf{g} \quad t \in (0, MT], \mathbf{x} \in \Gamma_{in}, \quad (1c)$$

$$-\bar{p}\mathbf{n} + \nu \mathbf{S}(\bar{\mathbf{u}})\mathbf{n} - \boldsymbol{\tau}^d(\bar{\mathbf{u}})\mathbf{n} = \mathbf{0} \quad t \in (0, MT], \mathbf{x} \in \Gamma_{out}, \quad (1d)$$

with zero initial boundary condition for the velocity, and where M is the number of heartbeats, T the period of a heartbeat, $(\mathbf{u} \otimes \mathbf{u})_{ij} = u_i u_j$, $\mathbf{S}(\mathbf{u}) = \nabla \mathbf{u} + (\nabla \mathbf{u})^T$, Γ_{in} is the inlet, Γ_{out} the two outlets given by the iliac segments, ν is the kinematic viscosity, and $\mathbf{g}(t, \mathbf{x})$ is a given boundary data. In particular, at the inlet Γ_{in} we impose for all the three patients the representative time variation of the flow rate $Q(t)$ reported in Figure 1. The systolic Reynolds numbers at the inlet for the three cases are 1277, 1220, 1186, respectively. Here, the flow rate is defined as

$$Q = \int_{\Gamma_{in}} \bar{\mathbf{u}} \cdot \mathbf{n} d\sigma. \quad (2)$$

61 This is a defective boundary condition, since at each time step we are prescribing only a scalar quantity over
 62 the whole Γ_{in} . In order to fill this gap, we make the assumption of a parabolic velocity profile along the
 63 normal direction, yielding the Dirichlet condition (1c), \mathbf{g} being the unique function with a parabolic profile
 64 in the normal direction and vanishing in the tangential ones, with flow rate equal to $Q(t)$. No perturbation
 65 is prescribed, so that the flow is assumed to be laminar at the inlet boundary. This will allow us to capture
 transitional effects arising as a consequence of geometry and pulsatility solely.

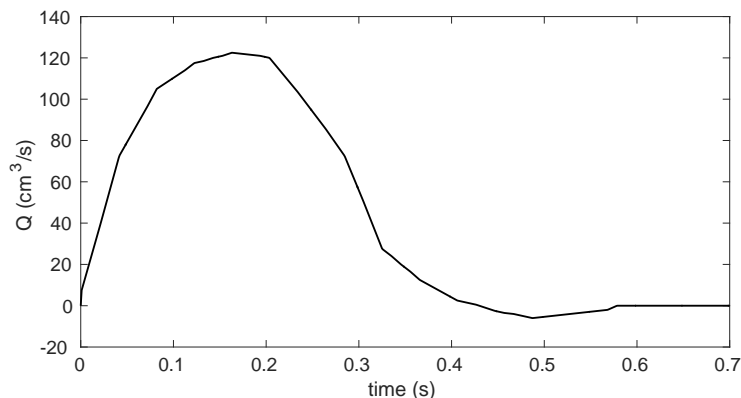


Figure 1: Flow waveform prescribed at the inlet.

66 The tensor $\boldsymbol{\tau}^d = \boldsymbol{\tau} - \frac{1}{3} \sum_k \tau_{kk} \mathbf{I}$ in (1) is the deviatoric part of the subgrid-scale tensor $\boldsymbol{\tau}$. The latter is suitably modeled as a function of the filtered quantities $\bar{\mathbf{u}}$, hence equations (1) have only $(\bar{\mathbf{u}}, \bar{p})$ as dependent variables. Usually, the effect of the subgrid-scale on the resolved scales is modeled in analogy with the kinetic theory of gases, by introducing a subgrid-scale viscosity ν_{sgs} and by modeling the deviatoric part of the subgrid-scale tensor as follows

$$\boldsymbol{\tau}^d(\bar{\mathbf{u}}) = -2\nu_{sgs}(\bar{\mathbf{u}}) \mathbf{S}(\bar{\mathbf{u}}).$$

The eddy viscosity model considered in this work is the σ -model, introduced in [18]. This is based on the introduction of the singular values $\sigma_1(t, \mathbf{x}) \geq \sigma_2(t, \mathbf{x}) \geq \sigma_3(t, \mathbf{x}) \geq 0$ of $\nabla \bar{\mathbf{u}}$, and on defining the subgrid-scale viscosity as follows:

$$\nu_{sgs} = C \bar{\Delta}^2 \frac{\sigma_3(\sigma_1 - \sigma_2)(\sigma_2 - \sigma_3)}{\sigma_1^2}, \quad (3)$$

67 where C is a suitable constant and $\bar{\Delta}$ the filter width. In our simulation we set $C = 1.5$ [18, 24]. For the
 68 grid filter we considered an *implicit* procedure [25], where the filter width $\bar{\Delta}$ represents the size of a mesh
 69 that is not able to capture all the scales [23]. This empirical choice is the most widely used nowadays.

70 As for the time discretization, we use a semi-implicit approach to linearize the momentum equation
 71 (1a), used in combination with a BDF2 scheme [26]. In particular, the convective field and the subgrid-
 72 scale viscosity have been evaluated by means of a second order extrapolation [24]. This treatment yields a
 73 CFL-like limitation on the time step Δt ($\Delta t \lesssim h$ [27]). For the space discretization we use Finite Elements
 74 with a SUPG stabilization term added to control numerical instabilities due to the large convective term
 75 [28]. We used $P2 - P2$ Finite Elements, that is piecewise quadratic polynomials for the approximation of

76 the pressure and each velocity component. A Pressure Stabilized Petrov-Galerkin (PSPG) formulation [28]
 77 was used to ensure the non-singularity of the corresponding matrix. For the description of the complete
 78 discretized-in-time problem, **WE REFER THE READER ELSEWHERE** [24].

79 We use the following data: physical viscosity $\nu = 0.033 \text{ cm}^2/\text{s}$, time discretization parameter $\Delta t =$
 80 0.001 s , number of heartbeats $M = 6$ and heartbeat period $T = 0.7 \text{ s}$.

81 All numerical results have been obtained using the parallel Finite Element library LIFEV (www.lifev.org).

82 2.3. Quantities of interest

83 To describe the blood dynamics and in particular transitional effects in the three AAA geometries, we
 84 introduce the following operators and post-processed quantities:

- *Ensemble-average*. Given a quantity $S(t, \mathbf{x})$, we define its ensemble-average as:

$$\langle S(t, \mathbf{x}) \rangle = \frac{1}{M} \sum_{j=1}^M S(t + (j-1)T, \mathbf{x}), \quad t \in (0, T].$$

This allows us to remove from the field of interest the random, zero-time-mean fluctuations due to the transitional effects appearing at each heartbeat. In this study, we consider the ensemble-average velocity magnitude $\langle U \rangle$ and wall shear stress $\langle WSS \rangle$, where

$$U(t, \mathbf{x}) = \|\bar{\mathbf{u}}(t, \mathbf{x})\|_{\mathbb{R}^3} \quad WSS(t, \mathbf{x}) = \nu \sqrt{\sum_{j=1}^2 (\nabla \bar{\mathbf{u}} \mathbf{n} \cdot \boldsymbol{\tau}^{(j)})^2}, \quad t \in (0, MT],$$

85 the latter quantity is computed on the lateral surface, \mathbf{n} is the outward unit vector, and $\boldsymbol{\tau}^{(j)}$, $j = 1, 2$,
 86 the tangential unit vectors;

- *Standard deviation of the fluctuations of the velocity magnitude*. This is defined as

$$SD(t, \mathbf{x}) = \sqrt{\frac{1}{M} \sum_{j=1}^M (U(t + (j-1)T, \mathbf{x}) - \langle U(t, \mathbf{x}) \rangle)^2}, \quad t \in (0, T].$$

87 This allows us to quantify and localize the velocity fluctuations among the heartbeats;

- *Q-criterion*. The scalar field Q is defined as

$$Q(t, \mathbf{x}) = -\frac{1}{2} \left(\sum_{i,j} S_{ij}^2(t, \mathbf{x}) - \Omega_{ij}^2(t, \mathbf{x}) \right), \quad t \in (0, MT],$$

88 where $\boldsymbol{\Omega} = \nabla \bar{\mathbf{u}} - (\nabla \bar{\mathbf{u}})^T$ [29, 14]. Positive values of Q indicate locations where rotations dominates
 89 over strain and shear. This allows us to identify regions where vortical structures are present;

- *Global Turbulent Kinetic Energy*. It is defined as the space integral of the Turbulent Kinetic Energy ($TKE(t, \mathbf{x})$) [11]:

$$k(t) = \frac{1}{2} \int_{\Omega} \frac{1}{M} \sum_{j=1}^M \left((\bar{u}_x(t + (j-1)T, \mathbf{x}) - \langle u_x(t, \mathbf{x}) \rangle)^2 + (\bar{u}_y(t + (j-1)T, \mathbf{x}) - \langle u_y(t, \mathbf{x}) \rangle)^2 + \right. \\ \left. (\bar{u}_z(t + (j-1)T, \mathbf{x}) - \langle u_z(t, \mathbf{x}) \rangle)^2 \right) d\mathbf{x}, \quad t \in (0, T].$$

90 TKE is representative of the cycle-to-cycle variation of the velocity field and its spatial average $k(t)$
 91 allows us to identify the temporal instants within the heartbeat where fluctuations in the whole AAA
 92 are more pronounced. Moreover, the average and maximum value of $k(t)$, here indicated as k_{mean} and
 93 k_{max} , respectively, are proposed in this study as synthetic indices to quantify the amount of variability
 94 of the velocity field in the aneurysmatic sac and thus the possible presence of transitional effects.

3. Results

3.1. Assessment of the computational meshes

The goal of LES simulations is to accurately describe turbulent flows on a coarser mesh than the one needed to perform a Direct Numerical Simulation (DNS), where all the significant scale of motions would need to be resolved. A suitable mesh for a LES model should be neither too fine, in order to be a valid alternative to DNS, nor too coarse, such that the assumptions underlying the LES model remain valid. To this aim, in this first set of simulations, we compare the results obtained for patient P1 with two meshes in order to estimate the number of tetrahedra of a reasonable mesh.

Referring to the results reported in Figure 2, we first observe that, as expected, blood flow is characterized by a jet that impinges on the distal part of the aneurysmatic sac (see figures at the top, where the ensemble-averaged velocity magnitude $\langle U \rangle$ over the 6 heartbeats has been plotted). Secondly, we observe an excellent qualitative agreement between $\langle U \rangle$ computed in the two meshes. This suggests that the coarser mesh is suitable for our purposes. This is also confirmed by the ratio between the subgrid-scale and molecular viscosities, reported in Figure 2, bottom. These figures clearly indicate the presence of transitional effects in the aneurysmatic sac, in particular at the mid-deceleration and early diastolic phases. The subgrid-scale viscosity reaches values up to five times the molecular one in the coarsest mesh and up to 3 times in the finest one. This means that the contribution of the subgrid-scale modeling is, as expected, greater for the coarsest mesh in order to account for the higher frequency cutoff introduced in this case by the implicit filter. At the same time, the numerical errors introduced by the coarsest mesh are still small enough not to compromise accuracy, since the results are in accordance with the finest mesh. For all these reasons, in what follows we consider for P2 and P3 meshes of the same level of refinement as the coarsest mesh used for P1.

3.2. Description of transitional effects

In Figure 3 we report for P2 and P3 the same quantities plotted in Figure 2 for P1, i.e. the ensemble-averaged velocity magnitude over 6 heartbeats and the ratio between the subgrid-scale and molecular viscosities. From these figures we observe again the jet impingement in the distal region of the aneurysmatic sac of P2. Instead, for P3 the non-axiality of the the tract of the aorta just above the sac forces the jet to impinge on the proximal part of the sac. Moreover, we observe that, as for P1, for both P2 and P3 the LES model is active, in particular during the mid-deceleration and early diastolic phases, with the subgrid-scale viscosity reaching values up to five times greater than those of the molecular viscosity.

In Figure 4, left, we report for all three cases the values of the standard deviation of the velocity magnitude over 6 heartbeats at the same three time instants as before. These plots show high values of the standard deviation for all the three cases at the early diastole and also at the mid-deceleration phase for P1 and P3. These values are of the same order of magnitude of the velocity itself (look at Figures 2 and 3). In the same figure, on the right, we plot the vortical structures identified by means of the Q -criterion. We have the formation of a vortex ring at the systolic peak which impinges the aneurysmatic sac at the mid-deceleration phase and, after the breakage, partially exits through the iliac outlets.

In Figure 5 we report the time evolution of the global Turbulent Kinetic Energy over 6 heartbeats for the three patients. We observe that, for all cases, the peak value is reached during the mid-deceleration phase ($t \simeq 0.3 - 0.4 s$). Moreover, we observe significant lower values for P2 with respect to P1 and P3, confirmed also by the mean and maximum in time values reported in Table 1, where we report also the dimensions of the three AAA.

The peak systolic Reynolds number for all the cases is computed as

$$Re = \frac{V_{sist} D}{\nu} = \frac{4Q_{sist}}{\pi D \nu} \simeq 2200,$$

where V_{sist} is the mean systolic velocity at the inlet, $Q_{sist} = 120 cm^3/s$ the systolic flow rate prescribed at the inlet (see Figure 1), and $D \simeq 2 cm$ a representative value, for all the patients, of the diameter at the inlet.

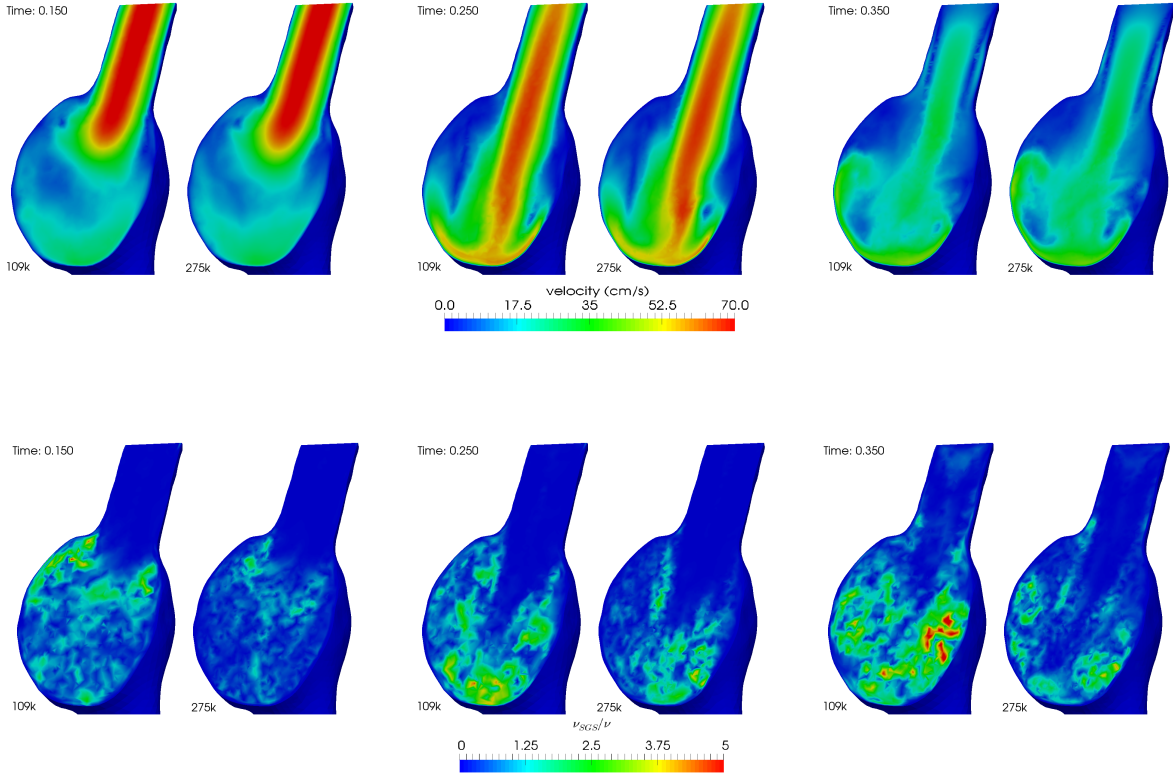


Figure 2: Top: Ensemble-averaged velocity magnitude over 6 heartbeats; Bottom: Ratio between the subgrid-scale and molecular viscosities. In each figure, we report on the left the results obtained with the coarse mesh and on the right those obtained with the fine mesh. Three time instants are reported: Systolic peak instant $t = 0.15$ s (left); Mid-deceleration $t = 0.25$ s (middle); Early diastole $t = 0.35$ s (right).

	P1	P2	P3
CC length	4.9	4.9	6.9
AP diameter	4.5	4.1	3.9
LL diameter	4.5	3.9	4.8
k_{mean}	19.0	13.2	21.0
k_{max}	46.8	32.1	47.2

Table 1: Values of the craniocaudal length (from the neck to the iliac outlets, in cm), of the antero-posterior and latero-lateral diameters (in cm), and of the mean and maximum in time of $k(t)$ (in cm^2/s^2).

140 Last, in Figure 6 we report the spatial distribution of the ensemble-averaged WSS over 6 heartbeats at
 141 the time instant where it reaches its maximum value ($t = 0.3$ s). From this figure, we observe large values
 142 in correspondance of the impingement regions.

143 4. Discussion

144 4.1. The presence of turbulence in abdominal aortic aneurysms and its clinical implications

145 The presence of turbulence in healthy vascular vessels seems to be confined to the ascending and thoracic
 146 aorta. However, these effects are quite negligible since, in physiological conditions, the helicity developed
 147 in such districts as a consequence of the ventricular contraction reduces the turbulent kinetic energy [30].
 148 A different situation occurs in pathological districts, where significant transition to turbulence effects could

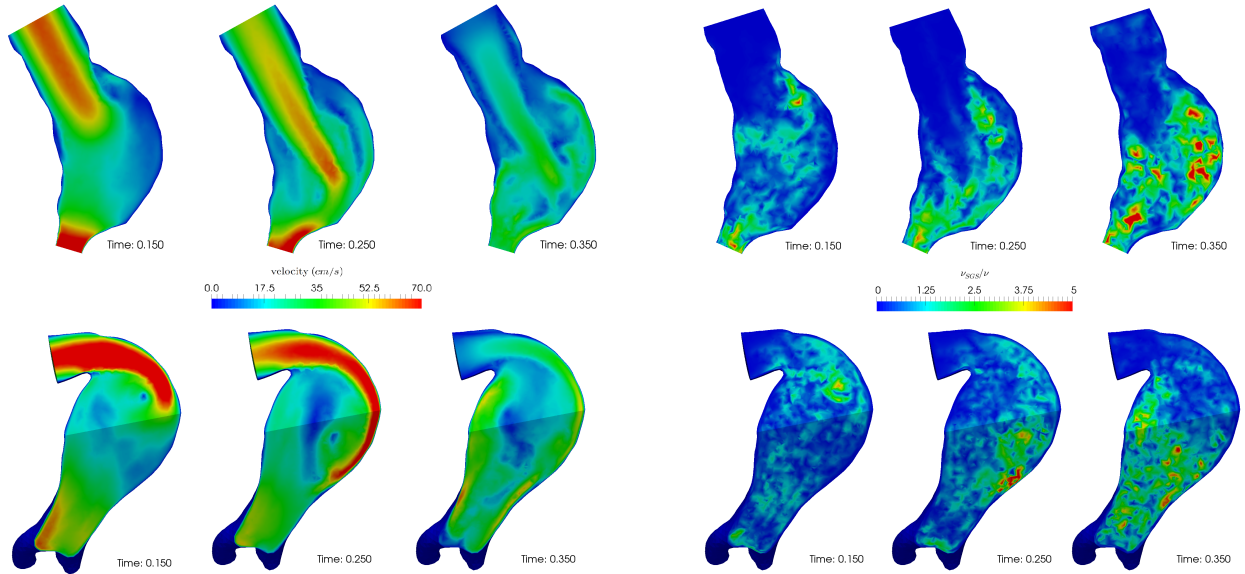


Figure 3: Left: Ensemble-averaged velocity magnitude over 6 heartbeats; Right: Ratio between the subgrid-scale and molecular viscosities. Top: Results for P2; Bottom: Results for P3. Three time instants are reported: Systolic peak instant $t = 0.15$ s (left); Mid-deceleration $t = 0.25$ s (middle); Early diastole $t = 0.35$ s (right).

149 develop, often as a consequence of a change of the geometry. For example, this is the case of stenotic carotids
 150 [12, 31, 32, 13, 14, 33, 34, 15].

151 Turbulence effects in abdominal aortic aneurysms due to the sudden change of geometric shape and to
 152 pulsatility have been observed in-vivo BY MEANS OF THE *Echo-Color Doppler (ECD) TECHNIQUE* [5]. Also
 153 in-vitro experiments in idealized AAA have been set up to study the presence of turbulence. IN PARTICULAR,
 154 ECD HAS BEEN USED TO HIGHLIGHT THE PRESENCE OF TURBULENCE IN STEADY CONDITIONS WHEN THE
 155 REYNOLDS NUMBER (Re) IS GREATER THAN 2250 [10, 35], A *laser Doppler velocimeter (LDV)* HAS
 156 REVEALED THE PRESENCE OF TURBULENCE UNDER STEADY EXERCISE CONDITIONS ($Re \simeq 4000$) [6], AND
 157 SIMILAR EXPERIMENTS HIGHLIGHTED THAT UNDER PULSATILITY CONDITIONS TURBULENCE MAY OCCUR
 158 AT LOWER Re VALUES (PEAK VALUE $Re \simeq 2300$) [36, 8, 37].

159 The presence of turbulence effects in AAA carries a significant clinical impact. In the initial phases
 160 of AAA DEVELOPMENT, turbulence interferes with endothelial cells turnover, which is at the basis of
 161 atherosclerosis development, also at relative low level of shear stresses [7]. This is probably due to high-
 162 frequency fluctuations, to the rapidly changing direction of shear stress, and to the comparable dimensions
 163 of the smallest turbulent eddies and endothelial cells. In the more advanced stages of AAA development,
 164 turbulence produces increased wall shear stresses compared with laminar flows, which may be responsible for
 165 further aneurysm dilatation, since the abdominal aorta regulates its diameter to maintain the shear stress
 166 below a physiological value [38]. Moreover, the increased shear stresses together with aortic wall vibration
 167 due to the large fluctuations, could damage the vessel wall, with possible implications on aneurysm growth
 168 and rupture [39, 10]. Finally, turbulent flows probably damage blood platelets promoting the formation of
 169 intraluminal thrombus (ILT) inside the aneurysmatic sac [3, 8].

170 4.2. Overview of computational studies

171 For all these reasons, some authors included the analysis of turbulence and/or transitional effects in
 172 their studies of blood dynamics in AAA. RIGID IDEAL GEOMETRIES UNDER STEADY CONDITIONS HAVE
 173 BEEN CONSIDERED [40, 10], where the increase of turbulent fluctuations in the distal part of the aneurysm
 174 has been reported, whereas the analysis for similar geometries and under pulsatile physiological conditions
 175 revealed the presence of vortices detaching from the wall and travelling towards the distal neck [36, 9]. The

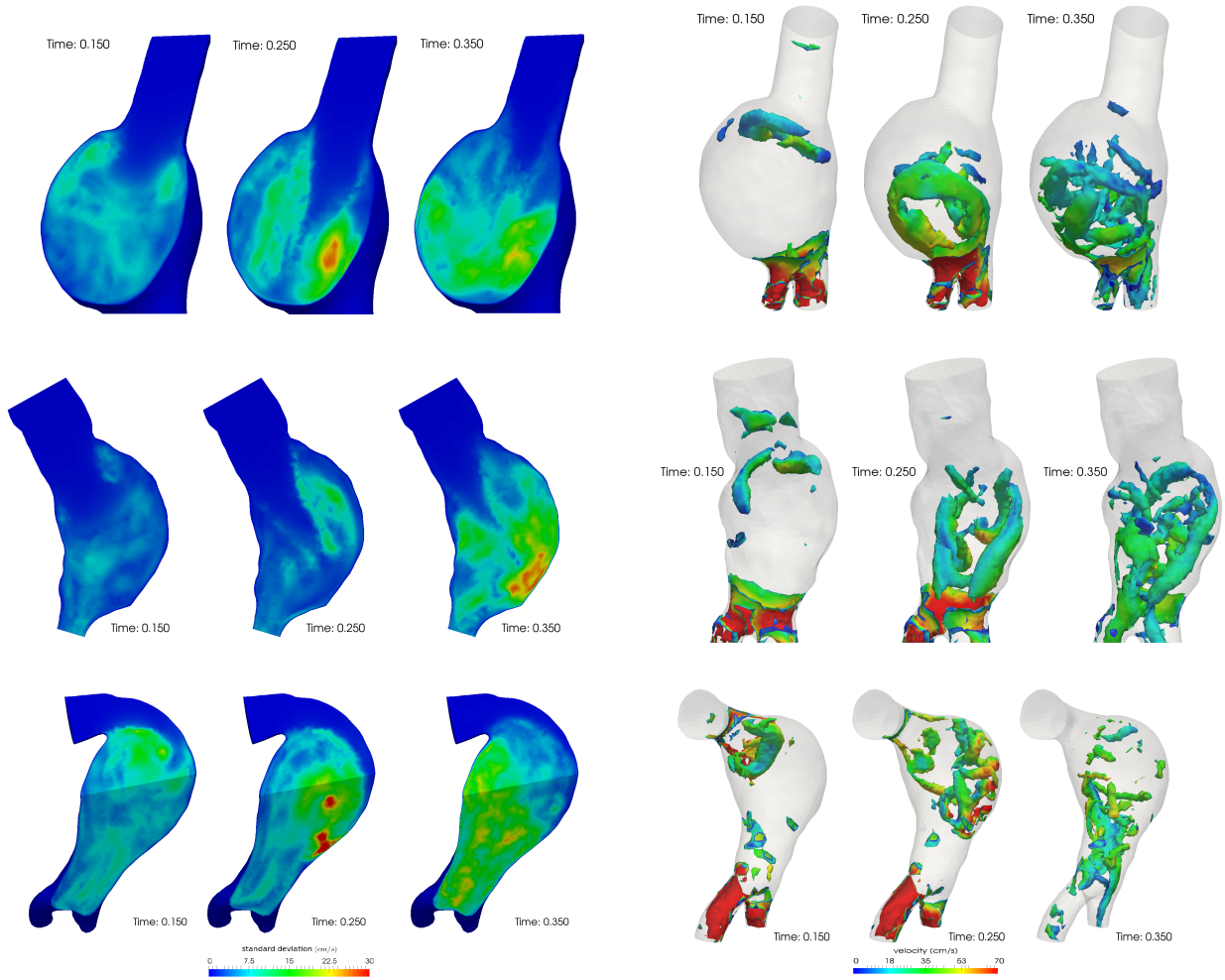


Figure 4: Left: Standard deviation of the velocity magnitude over 6 heartbeats. Right: Q-criterion (we report the regions with $Q > 5000$ painted by the velocity magnitude). Top: Results for P1; Middle: Results for P2; Bottom: Results for P3. Three time instants are reported for each case: Systolic peak instant $t = 0.15$ s; Mid-deceleration $t = 0.25$ s; Early diastole $t = 0.35$ s.

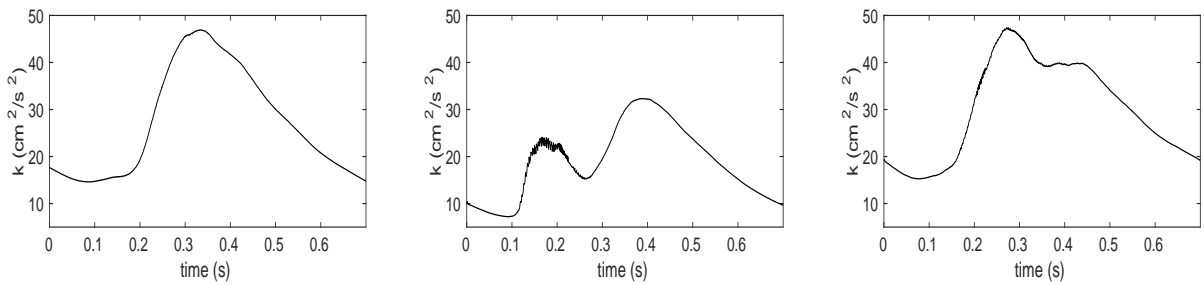


Figure 5: Global Turbulent Kinetic Energy $k(t)$ over 6 heartbeats for the three patients. Left: P1; Middle: P2; Right: P3.

176 inclusion of the aortic wall deformation in ideal AAA geometries resulting in a fluid-structure interaction
 177 analysis has been also considered for the study of turbulence effects [41]. Studies of turbulence effects in
 178 realistic AAA geometries reconstructed by radiological images have been carried out, reporting the influence
 179 of exercise conditions [11] and highlighting the relationship of such effects with the thrombus formation [3].

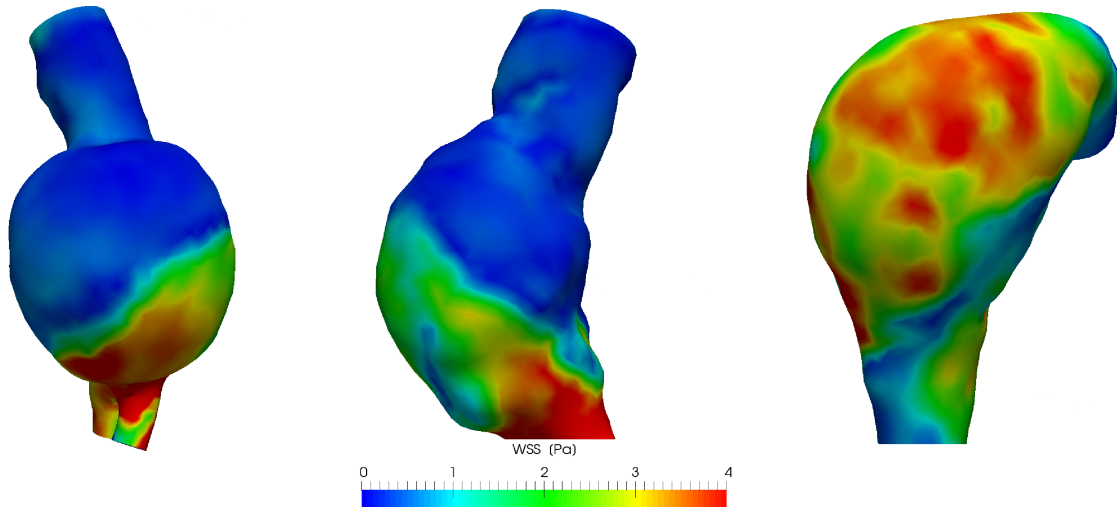


Figure 6: Peak ensemble-averaged Wall Shear Stress over 6 heartbeats ($t = 0.3 s$). Left: P1; Middle: P2; Right: P3.

180 Regarding the turbulent models included in these studies, the $k - \varepsilon$ [9] and $k - \omega$ [41] models were
 181 also considered, whereas a *Direct Numerical Simulation* WAS REALIZED ELSEWHERE [11]. A LES model
 182 implemented in a commercial software was also used [42, 43]; however no information on the LES model
 183 was provided and no analysis of turbulence was reported, the focus of these papers being the influence of
 184 boundary conditions and the monocyte deposition, respectively.

185 One of the major difficulties in computational models relies on a proper definition of suitable quantities
 186 capable to describe and quantify the turbulent and transitional effects in AAA. Often, the presence of such
 187 effects has been simply related to the formation of vortices and disturbed flow. However, some authors
 188 provided more statistically-sound quantities to assess turbulence in AAA. The standard deviation of the
 189 velocity field has been computed to assess and localize the presence of velocity fluctuations [10], whereas the
 190 Turbulent Kinetic Energy has been reported as a similar quantification of turbulent instabilities [41, 11].

191 4.3. Discussion of the methods

192 In this study we considered a LES model implemented in the Finite Element library LIFEV. In particular,
 193 we used the eddy viscosity σ -model, which vanishes in the cases of pure rotation, pure shear, or when the
 194 resolved scales are in axisymmetric or isotropic expansion. Moreover, the turbulent stresses decay as the
 195 distance to the solid boundary to the third power [18]. These features make the σ -model suitable to
 196 simulate fluids in enclosed domains and in presence of shear layers as in the present case. In principle, the
 197 model is well suited to describe cases (like the present one) where both spatial and temporal instabilities
 198 are present. For these reasons, it has been successfully applied to describe ventricular blood dynamics [44].
 199 Our implementation of the σ - model HAS BEEN VALIDATED ELSEWHERE [24], where a comparison with a
 200 DNS solution highlighted the accuracy of this LES model when used in coarse meshes of stenotic carotids.

201 Blood has been modeled as a constant density, Newtonian, and homogeneous fluid, a well-accepted
 202 hypothesis in the previous studies of turbulence effects in AAA [41, 11, 3]. However, we observe that the
 203 Newtonian hypothesis may be considered as a limitation of the present study, since the small eddies arising
 204 as a consequence of turbulent or transitional effects may justify the use of a non-Newtonian rheology [9]. We
 205 also assumed rigid walls, another well accepted hypothesis in this context [9, 11, 3], which however represents
 206 in fact a second limitation of the present work. Indeed, some differences with respect to the complete fluid-
 207 structure interaction (FSI) model have been highlighted [9]. In particular, the rigid wall assumption seems to
 208 slightly overestimate the turbulence kinetic energy. Regarding boundary conditions, in absence of measures,
 209 we prescribed a representative flow rate at the inlet, whereas zero stresses are set at the iliac outlets. The
 210 latter conditions could be justified by noticing that the resistance downstream the two iliac tracts should

211 be equal in physiological conditions. However, the prescription of patient-specific velocity data **OBTAINED,**
 212 **FOR EXAMPLE,** by the *phase-contrast-MRI* technology could provide more accurate results, as highlighted
 213 also for AAA [42]. Alternatively, at the outlets boundary conditions based on 3-element windkessel models
 214 may be considered for AAA [11]. We also observe that at the inlet we selected a priori a parabolic velocity
 215 profile to prescribe the defective flow rate condition (2). This is one the major limitations of the present
 216 work. Indeed, this choice could have an impact on the solution if the inlet region is not extended enough to
 217 allow the velocity profile to reach a fully developed state. To overcome this drawback, Lagrange multipliers
 218 [45, 46], optimal control [47], or Nitsche [48, 49] approaches could be used to reduce the impact on the
 219 solution [50]. Moreover, from radiological dynamic images, it has been observed that blood flow after the
 220 thoracic tract is markedly three-dimensional with secondary flows generated by the torsion and curvature
 221 of the aorta [51, 52].

222 Despite these drawbacks, in this first study on transitional effects in AAA, we decided to assume a
 223 Newtonian rheology and rigid-walls, together with simplified boundary conditions. Since the main focus of
 224 the present study is on the suitability of LES models in AAA geometries, we believe that these potential
 225 sources of inaccuracy should not influence the general trends and conclusions of the results we are going
 226 to discuss in the next subsection. Of course, we are working to relax them, in order to include FSI, non-
 227 Newtonian, and more-realistic boundary conditions in our future studies.

228 4.4. Analysis of the results

229 Although many authors speak about *turbulence* in AAA, here we prefer to refer to instability processes
 230 as *transition to turbulence*: the pulsatility of the blood flow on the one hand is responsible for instabilities
 231 occurring at lower Reynolds number than in the steady case [10, 8], while on the other hand does not allow
 232 the complete development of the flow into the turbulent regime. This is prevented by the acceleration phase
 233 of a new heartbeat that laminarizes the flow [8].

234 From our results, we can state that transitional effects are significant in AAA, as confirmed by the large
 235 values of the standard deviation of the velocity magnitude (up to 40% of the velocity magnitude itself, see
 236 Figure 4, left). This means that the velocity field presents significant random fluctuations among different
 237 heartbeats. By looking at Figures 2, 3, 4, and 5 we observe all reported quantities related to the formation
 238 of transitional effects (i.e. the ratio between subgrid-scale and molecular viscosities, the standard deviation
 239 of the velocity magnitude, the Q-criterion, and the global KTE) being higher during the mid-deceleration
 240 phase. This confirms previous observations that at similar Reynolds numbers the flow tends to be very
 241 unstable at the beginning of the deceleration [8]. In particular, we find that during the mid-deceleration
 242 phase, the flow jet impinges on the aneurysmatic sac creating recirculation regions around the impingement
 243 point that propagates proximally around the jet and distally through the iliac outlets. These instabilities
 244 are well captured by the distribution of the standard deviation of the velocity magnitude.

245 Referring to Figures 2, 3, 4, left, we observe that for all the three patients, the regions with elevated
 246 values of the subgrid-scale viscosity are in fact those of disturbed flow (high standard deviation of the velocity
 247 magnitude). This confirms the suitability of the σ -LES model in this context, being able to turn on only
 248 where and when needed, with values of the subgrid-scale viscosity reaching up to five times the molecular
 249 one. On the other hand, the LES model switches itself essentially off in the laminar regions.

250 As noticed by observing Figure 4, right, blood flow is characterized by a vortex ring that originates at
 251 the neck of the aneurysm, where a sudden change of diameter occurs. This ring propagates towards the
 252 inner region of the aneurysmatic sac and breaks down after the impingement. This phenomenon, at the
 253 best of our knowledge observed here for the first time in AAA, seems to be very similar to that taking place
 254 in the left ventricle and due to the passage of blood flow through the mitral valve [53, 54]. However, some
 255 differences are notable. First, the breakage of the vortex ring in AAA is due to the impingement, whereas
 256 in the heart it occurs in the middle of the ventricle chamber. This is probably due to the presence in AAA
 257 of outlets in the opposite direction of the entrance region. This, unlike the left ventricle featuring no outlets
 258 during the diastolic filling, helps the propagation of the ring towards the distal part of the sac. Moreover,
 259 as highlighted by the figures on the right ($t = 0.35$ s), during the diastolic phase the vortex ring transforms
 260 into a swirling structure after the impingement. Again, this should be caused by the presence of the iliac
 261 outlets that favour the exit of the flow structures.

262 Analyzing Figure 5, we observe that the global Turbulent Kinetic Energy is clearly lower for P2 than
263 for P1 and P3. This is also confirmed by the results reported in Table 3.2, highlighting that both k_{mean}
264 and k_{max} decrease for P2 by more than 30%. By considering these results together with the dimensions of
265 the aneurysms, we observe that P2 is characterized by smaller dimensions of the sac. Possible correlations
266 between the AAA dimensions and the intensity of the global Turbulent Kinetic Energy deserves a particular
267 attention for future studies. We also observe periodic flow instabilities in Patient 2 which are very similar
268 **TO THOSE OBSERVED IN CEREBRAL ANEURYSMS [17].**

269 Finally, from Figure 6 we observe that the higher values of the peak ensemble-averaged WSS are localized
270 at the mid-deceleration phase and in the regions of the impingement, that is where transitional effects occur.
271 **THESE ELEVATED VALUES ARE DUE TO THE IMPINGEMENT ITSELF, BUT PROBABLY THEY ALSO ASSUME**
272 **INCREASED VALUE WITH RESPECT TO THE LAMINAR CASE FOR THE PRESENCE OF TRANSITIONAL EFFECTS**
273 **[38, 10, 9].**

274 5. Conclusions

275 In this study, for the first time a large eddy simulation model has been used to study effects related to
276 transition to turbulence in abdominal aortic aneurysms. We found that the considered LES model is capable
277 to turn itself on in regions where the instabilities and fluctuations occur, i.e. around the impingement region
278 at the mid-deceleration phase. Transitional effects were studied by computing the standard deviation of
279 the velocity magnitude and the Q-criterion. The latter quantity highlighted the presence of a vortex ring
280 that starts from the neck of the aneurysmatic sac and propagates within this. After its breakage due to
281 the impingement, this annular structure transforms into a swirling flow that exits through the outlets. Our
282 results also suggested a strong correlation between the dimensions of the AAA and the intensity of the
283 Turbulent Kinetic Energy.

284 Conflicts of interest

285 None declared.

286 Sources of funding for this research

287 CV and LF have been partially supported by the Italian MIUR PRIN12 project no. 201289A4LX
288 “Modelli matematici e numerici del sistema cardiocircolatorio e loro applicazione in ambito clinico”. CV
289 was also partially supported by INDAM-GNCS. DLV has been supported by the ERC 2015 Proof of Concept
290 “math4AAArisk” (A mathematical platform for Abdominal Aortic Aneurism risk assessment and surgical
291 planning).

292 Ethical approval

293 We obtained the Authorisation from the Chief medical Officer of I.R.C.C.S. Fondazione Ca Granda
294 Policlinico Ospedale Maggiore di Milano - Prot. 2863 04.01.2013.

295 References

- 296 [1] C. Fleming, E. Whitlock, T. Beil, F. Lederle, Screening for Abdominal Aortic Aneurysm: A Best-Evidence Systematic
297 Review for the U.S. Preventive Services Task Force, *Ann Intern Med* 142(3) (2005) 203–211.
- 298 [2] E. Bagci, Y. Vodovotz, T. Billiar, B. Ermentrout, I. Bahar, Computational Insights on the Competing Effects of Nitric
299 Oxide in Regulating Apoptosis, *PLOS One* 3(5) (2008) e2249.
- 300 [3] M. O’Rourke, J. McCullough, S. Kelly, An investigation of the relationship between hemodynamics and thrombus deposi-
301 tion within patient-specific models of abdominal aortic aneurysm, *Proceedings of the Institution of Mechanical Engineers,*
302 *Part H: Journal of Engineering in Medicine* 226(7) (2012) 548–564.

- 303 [4] M. Piccinelli, C. Vergara, L. Antiga, L. Forzenigo, P. Biondetti, M. Domanin, Impact of hemodynamics on lumen bound-
304 ary displacements in abdominal aortic aneurysms by means of dynamic computed tomography and computational fluid
305 dynamics, *Biomech Model Mechanobiol* 12(6) (2013) 1263–1276.
- 306 [5] E. Bluth, S. Murphey, L. Hollier, M. Sullivan, Color flow Doppler in the evaluation of aortic aneurysms, *Int Angiol* (9(1))
307 (1990) 8–10.
- 308 [6] C. Egelhoff, R. Budwig, D. Elger, T. Khraishi, K. Johansen, Model studies of the flow in abdominal aortic aneurysms
309 during resting and exercise conditions, *Journal of Biomechanics* 32 (12) (1999) 13191329.
- 310 [7] P. Davies, A. Remuzzi, E. Gordon, C. D. Jr, M. G. Jr, Turbulent fluid shear stress induces vascular endothelial cell turnover
311 in vitro, *Proceedings of the National Academy of Sciences of the United States of America* 83 (7) (1986) 2114–2117.
- 312 [8] T. Yip, S. Yu, Cyclic transition to turbulence in rigid abdominal aortic aneurysm models, *Fluid Dynamics Research* 29 (2)
313 (2001) 81–113.
- 314 [9] K. Khanafer, J. Bull, G. U. Jr., R. Berguer, Turbulence Significantly Increases Pressure and Fluid Shear Stress in an
315 Aortic Aneurysm Model under Resting and Exercise Flow Conditions, *Annals of Vascular Surgery* 21 (1) (2007) 67–74.
- 316 [10] C. Asbury, J. Ruberti, E. Bluth, R. Peattie, Experimental investigation of steady flow in rigid models of abdominal aortic
317 aneurysms, *Annals of Biomedical Engineering* 23 (1) (1995) 29–39.
- 318 [11] A. Les, S. Shadden, C. Figueroa, J. Park, M. Tedesco, R. Herfkens, R. Dalman, C. Taylor, Quantification of Hemodynamics
319 in Abdominal Aortic Aneurysms During Rest and Exercise Using Magnetic Resonance Imaging and Computational Fluid
320 Dynamics, *Annals of Biomedical Engineering* 38 (4) (2010) 12881313.
- 321 [12] J. Stroud, S. Berger, D. Saloner, Numerical Analysis of Flow Through a Severely Stenotic Carotid Artery Bifurcation, *J*
322 *Biomech Eng* 124 (1) (2002) 9–20.
- 323 [13] L. Grinberg, A. Yakhov, G. Karniadakis, Analyzing Transient Turbulence in a Stenosed Carotid Artery by Proper Or-
324 thogonal Decomposition, *Annals of Biomedical Engineering* 37 (11) (2009) 2200–2217.
- 325 [14] S. Lee, S. Lee, P. Fischer, H. Bassiouny, F. Loth, Direct numerical simulation of transitional flow in a stenosed carotid
326 bifurcation, *J Biomech* 41 (11) (2008) 2551–2561.
- 327 [15] V. Rayz, S. Berger, D. Saloner, Transitional flows in arterial fluid dynamics, *Computer Methods in Applied Mechanics*
328 *and Engineering* 196 (31–32) (2007) 3043–3048.
- 329 [16] T. Yagi, A. Sato, M. Shinke, S. Takahashi, Y. Tobe, H. Takao, Y. Murayama, M. Umezu, Experimental insights into flow
330 impingement in cerebral aneurysm by stereoscopic particle image velocimetry: transition from a laminar regime, *Journal*
331 *of Biomechanics* 10 (82).
- 332 [17] M. Khan, C. Chnafa, D. Gallo, F. Molinari, U. Morbiducci, D. Steinman, K. Valen-Sendstad, On the quantification
333 and visualization of transient periodic instabilities in pulsatile flows, *Journal of Biomechanics* 52 (2017) 179–182.
- 334 [18] F. Nicoud, H. B. Toda, O. Cabrit, S. Bose, J. Lee, Using singular values to build a subgrid-scale model for large eddy
335 simulations, *Physics of Fluids* 23 (8) (2011) 085106.
- 336 [19] L. Antiga, D. Steinman, *The Vascular Modeling Toolkit (VMTK)*, 2009.
- 337 [20] A. Quarteroni, A. Manzoni, C. Vergara, *The cardiovascular system: Mathematical modelling, numerical algorithms and*
338 *clinical applications*, *Acta Numerica* 26 (2017) 365–590.
- 339 [21] R. Rogallo, P. Moin, Numerical Simulation of Turbulent Flows, *Annual Review of Fluid Mechanics* 16 (1984) 99–137.
- 340 [22] J. Smagorinsky, General circulation experiments with the primitive equations: I. The basic experiment, *Monthly weather*
341 *review* 91 (1963) 99–164.
- 342 [23] S. Pope, *Turbulent flows*, Cambridge University Press, 2000.
- 343 [24] R. Lancellotti, C. Vergara, L. Valdetaro, S. Bose, A. Quarteroni, Large eddy simulations for blood dynamics in realistic
344 stenotic carotids, *Int. J. Numer. Meth. Biomed. Eng.* DOI: 10.1002/cnm.2868.
- 345 [25] J. Deardorff, A numerical study of three-dimensional turbulent channel flow at large Reynolds numbers, *Journal of Fluid*
346 *Mechanics* 41 (1970) 453–465.
- 347 [26] E. Hairer, S. Nørsett, G. Wanner, *Solving ordinary differential equations: Nonstiff problems*, Springer Series in Comput.
348 *Math.*, Springer, ISBN 9783540566700, 1993.
- 349 [27] A. Quarteroni, A. Valli, *Numerical approximation of partial differential equations*, Springer, 1994.
- 350 [28] T. Tezduyar, Stabilized finite element formulations for incompressible flow computations, *Advances in Applied Mathe-*
351 *matics* 28 (1992) 1–44.
- 352 [29] C. Chong, Perry, A general classification of three-dimensional flow fields, *Phys Fluids A* 2 (1990) 765.
- 353 [30] U. Morbiducci, R. Ponzini, G. Rizzo, M. Cadioli, A. Esposito, F. Montecchi, A. Redaelli, Mechanistic insight into
354 the physiological relevance of helical blood flow in the human aorta: an in vivo study, *Biomechanics and Modeling in*
355 *Mechanobiology* 10(3) (2011) 339–355.
- 356 [31] D. Birchall, A. Zaman, J. Hacker, G. Davies, D. Mendelow, Analysis of haemodynamic disturbance in the atherosclerotic
357 carotid artery using computational fluid dynamics, *European Radiology* 16 (5) (2006) 1074–1083.
- 358 [32] F. Tan, G. Soloperto, S. Bashford, N. Wood, S. Thom, A. Hughes, X. Xu, Analysis of Flow Disturbance in a Stenosed
359 Carotid Artery Bifurcation Using Two-Equation Transitional and Turbulence Models, *J Biomech Eng* 130 (6) (2008)
360 061008.
- 361 [33] P. Fischer, F. Loth, S. Lee, S. Lee, D. Smith, H. Bassiouny, Simulation of high-Reynolds number vascular flows, *Comput.*
362 *Methods Appl. Mech. Engrg.* 196 (2007) 3049–3060.
- 363 [34] S. Cheung, K. K. L. Wong, G. H. Yeoh, W. Yang, J. Tu, R. Beare, T. Phan, Experimental and numerical study on the
364 hemodynamics of stenosed carotid bifurcation, *Australasian Physical & Engineering Sciences in Medicine* 33 (4) (2010)
365 319–328.
- 366 [35] R. Peattie, C. Asbury, E. Bluth, J. Ruberti, Steady flow in models of abdominal aortic aneurysms. Part I: Investigation
367 of the velocity patterns, *J Ultrasound Med* 15 (10) (1996) 679–688.

- 368 [36] T. Fukushima, T. Matsuzawa, T. Homma, Cyclic transition to turbulence in rigid abdominal aortic aneurysm models,
369 *Biorheology* 26 (2) (1988) 109–130.
- 370 [37] R. Peattie, T. Riehle, E. Bluth, Pulsatile Flow in Fusiform Models of Abdominal Aortic Aneurysms: Flow Fields, Velocity
371 Patterns and Flow-Induced Wall Stresses, *J Biomech Eng* 126 (4) (2004) 438–446.
- 372 [38] D. Giddens, C. Zarins, S. Glagov, Response of Arteries to Near-Wall Fluid Dynamic Behavior, *Applied Mechanics Reviews*
373 43 (5S) (1990) S98–S102.
- 374 [39] K. Johansen, Aneurysms, *Scientific American* 247 (1) (1982) 110–125.
- 375 [40] R. Budwig, D. Elger, H. Hooper, J. Slippy, Steady Flow in Abdominal Aortic Aneurysm Models, *J Biomech Eng* 115
376 (1993) 418–423.
- 377 [41] K. Khanafer, J. Bull, R. Berguer, Fluid-structure interaction of turbulent pulsatile flow within a flexible wall axisymmetric
378 aortic aneurysm model, *European Journal of Mechanics - B/Fluids* 28 (1) (2009) 88–102.
- 379 [42] D. Hardman, S. Semple, J. Richards, P. Hoskins, Comparison of patient-specific inlet boundary conditions in the numerical
380 modelling of blood flow in abdominal aortic aneurysm disease, *Int. J. Numer. Meth. Biomed. Engng.* 29 (2013) 165178.
- 381 [43] D. Hardman, B. Doyle, S. Semple, J. Richards, D. Newby, W. Easson, P. Hoskins, On the prediction of monocyte deposition
382 in abdominal aortic aneurysms using computational fluid dynamics, *Proceedings of the Institution of Mechanical Engineers,*
383 *Part H: Journal of Engineering in Medicine* 227 (10) (2013) 1114–1124.
- 384 [44] C. Chnafa, S. Mendez, F. Nicoud, Image-based large-eddy simulation in a realistic left heart, *Computers & Fluids* 94
385 (2014) 173–187.
- 386 [45] L. Formaggia, J. Gerbeau, F. Nobile, A. Quarteroni, Numerical treatment of Defective Boundary Conditions for the
387 Navier-Stokes equation, *SIAM Journal on Numerical Analysis* 40(1) (2002) 376–401.
- 388 [46] A. Veneziani, C. Vergara, Flow rate defective boundary conditions in haemodynamics simulations, *International Journal*
389 *for Numerical Methods in Fluids* 47 (2005) 803–816.
- 390 [47] L. Formaggia, A. Veneziani, C. Vergara, A new approach to numerical solution of defective boundary value problems in
391 incompressible fluid dynamics, *SIAM Journal on Numerical Analysis* 46(6) (2008) 2769–2794.
- 392 [48] P. Zunino, Numerical approximation of incompressible flows with net flux defective boundary conditions by means of
393 penalty technique, *Computer Methods in Applied Mechanics and Engineering* 198(37-40) (2009) 3026–3038.
- 394 [49] C. Vergara, Nitsche’s Method for Defective Boundary Value Problems in Incompressible Fluid-dynamics, *J Sci Comp*
395 46(1) (2011) 100–123.
- 396 [50] L. Formaggia, C. Vergara, Prescription of General Defective Boundary Conditions in Fluid-Dynamics, *Milan Journal of*
397 *Mathematics* 80(2) (2012) 333–350.
- 398 [51] M. Markl, M. Draney, D. Miller, J. Levin, E. Williamson, N. Pelc, D. Liang, R. Herfkens, Time-resolved three-dimensional
399 magnetic resonance velocity mapping of aortic flow in healthy volunteers and patients after valve-sparing aortic root
400 replacement, *The Journal of Thoracic and Cardiovascular Surgery* 130 (2) (2005) 456463.
- 401 [52] U. Morbiducci, R. Ponzini, D. Gallo, C. Bignardi, G. Rizzo, Inflow boundary conditions for image-based computational
402 hemodynamics: Impact of idealized versus measured velocity profiles in the human aorta, *Journal of Biomechanics* 46(1)
403 (2013) 102–109.
- 404 [53] J. Seo, V. Vedula, T. Abraham, A. Lardo, F. Dawoud, H. Luo, R. Mittal, Effect of the mitral valve on diastolic flow
405 patterns, *Physics of fluids* 26 (12) (2014) 121901.
- 406 [54] R. Mittal, J. Seo, V. Vedula, Y. Choi, H. Liu, H. Huang, S. Jain, L. Younes, T. Abraham, R. George, Computational
407 modeling of cardiac hemodynamics: Current status and future outlook, *Journal of Computational Physics* 305 (2016)
408 1065–1082.